

Spatially Resolved Galaxy Star Formation and its Environmental Dependence I

Niraj Welikala¹, Andrew J. Connolly², Andrew M. Hopkins³, Ryan Scranton¹, Alberto Conti⁴

ABSTRACT

We use the photometric information contained in individual pixels of 44,964 ($0.019 < z < 0.125$ and $-23.5 < M_r < -20.5$) galaxies in the Fourth Data Release (DR4) of the Sloan Digital Sky Survey to investigate the effects of environment on galaxy star formation (SF). We use the pixel- z technique, which combines stellar population synthesis models with photometric redshift template fitting on the scale of individual pixels in galaxy images. Spectral energy distributions are constructed, sampling a wide range of properties such as age, star formation rate (SFR), dust obscuration and metallicity. By summing the SFRs in the pixels, we demonstrate that the distribution of total galaxy SFR shifts to lower values as the local density of surrounding galaxies increases, as found in other studies. The effect is most prominent in the galaxies with the highest star formation, and we see the break in the SFR-density relation at a local galaxy density of $\approx 0.05 (\text{Mpc}/h)^{-3}$. Since our method allows us to spatially resolve the SF distribution within galaxies, we can calculate the mean SFR of each galaxy as a function of radius. We find that on average the mean SFR is dominated by SF in the central regions of galaxies, and that the trend for suppression of SFR in high density environments is driven by a reduction in this nuclear SF. We also find that the mean SFR in the outskirts is largely independent of environmental effects. This trend in the mean SFR is shared by galaxies which are highly star forming, while those which are weakly star forming show no statistically significant correlation between their environment and the mean SFR at any radius.

¹Department of Physics and Astronomy, University of Pittsburgh, 3941, O'Hara Street, Pittsburgh, PA 15260, USA, welikala@phyast.pitt.edu

²Department of Astronomy, University of Washington, Box 351580, Seattle, WA 98195-1580, USA, ajc@astro.washington.edu

³School of Physics, University of Sydney, NSW 2006, Australia, ahopkins@physics.usyd.edu.au

⁴Space Telescope Science Institute, Baltimore, MD 21218, USA

Subject headings: cosmology:observations — galaxies:distances and redshifts – galaxies:evolution– galaxies:formation

1. Introduction

1.1. Environmental dependences of galaxy properties and dependence on morphology

According to models of hierarchical formation (Kauffmann et al. 1993; Somerville & Primack 1999; Cole et al. 2000), galaxies form in less dense environments and are then accreted into larger halos (e.g., falling into clusters or groups), having their hot gas reservoir removed as this occurs. This predicts that galaxy properties, such as color, luminosity and SFR, are correlated with their environment. Galaxies in highly dense regions are predicted to be more luminous and more red than those in lesser dense regions. In fact, the mean galaxy environment as a function of color and luminosity has been explored using the Sloan Digital Sky Survey (SDSS) (Hogg et al. 2003; Blanton et al. 2003), as was the dependence of the color-magnitude relation of bulge-dominated galaxies on their environment (Hogg et al. 2004). The models also predict a gradual decrease in star formation (SF) activity in more dense regions, as seen in recent observational studies exploring the variation of star formation rate (SFR) with environment (Lewis et al. 2002; Gómez et al. 2003). Numerous physical mechanisms for how such SFR suppression might occur have been suggested, including ram pressure stripping of gas (Gunn & Gott 1972), gravitational interactions between galaxies (Byrd & Valtonen 1990) and between galaxies and a non-uniform cluster potential (“galaxy harassment,” Moore et al. 1999).

Recent N-body simulations and semi-analytical models have extended our insight into a number of the important issues with the hierarchical formation scenario. Balogh et al. (2000), investigating the origin of cluster-centric gradients in SFRs and colors of rich cluster galaxies, used a model where clusters are built through the ongoing accretion of field galaxies. These models assume that after galaxies enter the cluster their SFRs decline on a timescale of a few Gyr which is the typical gas consumption timescale for disk galaxies in the field. They combined these timescales with mass accretion histories from N-body simulations of cluster formation in a Λ CDM universe to show that there is an expected strong suppression of SF in cluster galaxies. The simulations also show that a significant fraction of galaxies beyond the virial radius of the cluster may have been within the main body of the cluster in the past. This would explain why star formation in the outskirts of clusters (and as far out as two virial radii) is systematically suppressed relative to the field. The agreement with the data beyond the cluster virial radius is further improved by assuming that gas-stripping

happens within lower mass systems, before the galaxy is actually accreted into the cluster. The suggestion is that the SFRs of cluster galaxies depend primarily on the time since their accretion onto the cluster, and that the SFR suppression happens gradually over a few Gyr.

Here we investigate the relation between environment and SFR for galaxies in the low redshift universe. Gómez et al. (2003), using $H\alpha$ equivalent widths (EW) as an indicator of SFR in the Early Data Release (EDR) of the SDSS, established an SFR-density relation for the SDSS, confirming a similar result seen in the 2 degree Field Galaxy Redshift Survey (2dFGRS) by Lewis et al. (2002). They found that the overall distribution of SFRs is shifted toward lower values in more dense environments. The effect is most noticeable for the strongly star-forming galaxies ($EW(H\alpha) > 5 \text{ \AA}$) in the 75th percentile of the SFR distribution. They also found a characteristic “break” (or characteristic density) in the density-SFR relation at a local galaxy density of $\approx 1 (\text{Mpc}/h)^{-2}$. Gómez et al. (2003) explored whether the density-morphology relation (Dressler 1980) alone could explain the density-SFR relation, and concluded that it could not. Using the concentration index of SDSS galaxies as a morphology indicator, they showed that SFRs for galaxies of the same type were suppressed in dense regions. Higher redshift samples ($z > 0.2$) have also been used to suggest a suppression in the SFR of galaxies in the cores of distant clusters compared to those in the field (Balogh et al. 1997; Hashimoto et al. 1998; Poggianti et al. 1999; Couch et al. 2001; Postman et al. 2001). Together this provides strong evidence for a decrease in SFR of galaxies in dense environments, spanning a wide range of densities ($0.08 - 10 (\text{Mpc}/h)^{-2}$) and redshift (out to $z \approx 0.5$). In addition, Balogh et al. (1997) and Hashimoto et al. (1998) found that cluster galaxies have a reduced SFR compared with the field, independent of morphology.

Not all studies agree with the general SFR-density trend though. Balogh et al. (2004) analyzed $H\alpha$ emission strength as a function of galaxy environment using galaxies selected from the SDSS and 2dFGRS. They found that the distribution of $H\alpha$ EWs is bimodal, consisting of actively star-forming populations with $EW(H\alpha) > 4 \text{ \AA}$ and a quiescent population with little current SF. They showed that the distribution of $EW(H\alpha)$ for the star forming population does not itself depend on environment, and concluded that it was unlikely that SFRs are gradually decreasing in a substantial number of star-forming galaxies in or near dense regions today. They did find, however, that the fraction of galaxies with $EW(H\alpha) > 4 \text{ \AA}$ decreases steadily with increasing local density.

1.2. Galaxy Evolution and environment

The most massive galaxies known today are giant ellipticals that reside in the most dense galaxy environments (e.g., Dressler 1980), which are also known to have formed their stars rapidly at an early stage in cosmic history. Recent studies of the evolution in the global space density of galaxy SFRs find that the majority of the observed SF occurs in the highest mass galaxies at high redshift, moving to lower mass galaxies at lower redshifts (Panter et al. 2004; Juneau et al. 2005; Panter et al. 2006; Seymour et al. 2007). This is referred to as “downsizing” (Cowie et al. 1996). Together with the trend for massive systems to occur predominantly in dense environments, this results in a scenario where the SFRs in dense environments at low redshift are lower than in less dense regions, consistent with the observations. The implication is that at sufficiently high redshifts, ($z \gtrsim 2$) where the SFR is dominated by the most massive galaxies, the SFR-density relation should invert, with the most dense environments hosting elevated SFRs compared to the field.

This trend is beginning to be observed too. Poggianti et al. (2006) show that at $0.4 < z < 0.8$ the suppression of SFR in dense environments is weaker than seen locally. Ilbert et al. (2006) and Elbaz et al. (2007) show environmental dependent evolution in the galaxy luminosity function from $0.25 < z < 1.5$, suggesting an increase in the density of faint red galaxies in overdense regions as cosmic time increases. More confirmation is clearly needed, of course, but these examples are consistent with the scenario that galaxies in dense environments form stars rapidly at early times, quickly building up mass and becoming quiescent, while galaxies in less dense environments form stars at a more sedate pace but over longer timescales.

This “environmentally governed evolution” scenario makes a distinct prediction compared to the “infall and quench” models. The latter suggests that galaxies in dense environments should show an SFR distribution that is progressively suppressed from the outside in, as the outer regions are those which will be affected first by their rapidly changing environment. The former, on the contrary, suggests that the suppression should either happen uniformly as a galaxy ages, or that the inner regions should be suppressed first, since nuclear SF seems to occur more rapidly than disk SF given the elevated gas densities present. Thus by studying the spatial distribution of SFR in star-forming galaxies as a function of environment we should be able to distinguish clearly between these two scenarios.

1.3. Radial Variation in Galaxy SFRs

Previous studies on the radial dependence of SF have focused on individual galaxies. Pérez-González et al. (2006) studied the recent SF in the early-type galaxy M81 using imaging observations from the far-ultraviolet (UV) to the far-infrared (IR). The data was then compared to models of stellar, gas and dust emission, with results from different sub-galactic regions, including individual HII regions (around 0.1 kpc). They were able to confirm the existence of a diffuse dust emission not directly linked to the SF. Using the $H\alpha$ emission that probes the unobscured SF, and the IR luminosity (especially the $24\ \mu\text{m}$ emission) that probes the obscured SF in the galaxy, they found a decrease in the ratio of obscured SF to total SF with radius. This fraction varies from an obscured SF of 60% in the inner regions of the galaxy to 30% in the outer regions. Johnston et al. (2005) used pixel-based spectral energy distribution (SED) fitting to a merging system hosting a compact steep spectrum radio source, in order to explore the connection between the nuclear radio emission and the distribution of star formation. Kassin, et al. (2003) used pixel-based colors to explore stellar populations and obscuration in the Antennae, and de Grijs et al. (2003) used the same technique to explore the Mice and the Tadpole interacting galaxy systems. Boissier et al. (2006) showed, using GALEX and Spitzer data, that for disk galaxies the attenuation varies radially, being highest in the nuclear regions, and is correlated with metallicity. They also found that the Schmidt law connecting the SF and gas surface densities continues beyond the traditional “threshold” radius. Lanyon-Foster et al. (2007) used a study of pixel Color Magnitude Diagrams for a sample of 69 nearby galaxies to study stellar populations and structure of galaxies. They found that these Color Magnitude Diagrams of each galaxy type have distinct trends. In addition, they performed a pixel-by-pixel analysis to show that there is a steady progression in average pixel color along the Hubble sequence. Finally they compared pixel colors to the Bruzual and Charlot stellar population models and used these to map the stellar mass distribution and M/L ratio in galaxies.

The current analysis has the advantage of a very large sample, accessible as a result of the SDSS, which allows a study of the environmental dependence of spatially distributed star formation. Also, since the inferred SFRs come from fitting SEDs, derived from stellar population synthesis models, to broadband photometry, there is no aperture effect such as that affecting fiber-based spectroscopy. By fitting SEDs to individual pixels within resolved galaxy images, we can spatially resolve the star formation and explore how this distribution varies for galaxies as a function of local galaxy density.

1.4. Using photometric redshifts to study (spatially-resolved) properties of stellar populations in galaxies

Photometric redshifts have become an efficient way of measuring redshifts of galaxies, particularly when the galaxies are too faint for spectroscopic studies. This typically involves fitting a library of SEDs to the observed colors of galaxies, where the SED templates are functions of galaxy type. We can, however, shift the focus from the inferred photometric redshifts themselves, to what the best fitting SEDs can reveal about the properties of the galaxy sample. This highlights instead the reliability and appropriateness of the template spectra used in the fitting. More specifically, as shown by Abraham (1998), the *spatially resolved* colors of galaxies can be used to understand the relative ages of bulge and disks and the formation histories of galaxies. This can be done by applying the photometric redshift technique to individual pixels of resolved galaxy images, having measured fluxes and flux errors. Given a library of SED templates constructed from population synthesis codes, for which the underlying physical parameters are defined, the spatial distribution of those parameters can then be established. Conti et al. (2003) applied such SED fitting, a technique referred to as “pixel-z,” to individual pixels in ≈ 150 galaxies with measured spectroscopic redshifts, and ≈ 1500 galaxies with measured photometric redshifts, in the Hubble Deep Field-North (HDF-N). The aim was to decompose the internal photometric structure of galaxies into intrinsic properties of the stellar populations like stellar ages and star formation rates. They used the pixels to calculate the comoving density of star formation and metallicity enrichment, as a function of redshift. With the sample of galaxies available, they were able to directly assess the drivers behind the current understanding of the global star formation history.

Here we apply the pixel-z technique to 44,964 SDSS galaxies, to study the dependence on environment of the total galaxy SFR and the spatial distribution of star formation within those galaxies. In § 2, we describe our SDSS sample. We describe the pixel-z method and its application to the SDSS in § 3, together with a description of the SEDs and the range of physical properties spanned. § 4 demonstrates features of the pixel-z implementation. § 5 presents our results, including the relation between total SFR and local density of galaxies, along with the spatial distribution of SFR as a function of this density. Our conclusions are described in § 6. We assume throughout that $\Omega_\Lambda = 0.7$, $\Omega_M = 0.3$, and $H_0 = 75 \text{ km s}^{-1} \text{ Mpc}^{-1}$.

2. Data

2.1. The Fourth Data Release of the Sloan Digital Sky Survey

The Sloan Digital Sky Survey (SDSS) is an imaging and spectroscopic survey of the sky using a dedicated 2.5m telescope (Gunn et al. 2006) at Apache Point Observatory in New Mexico. It aims to map a quarter of the sky, spanning the Northern Galactic Cap (York et al. 2000). Imaging is done in drift-scan mode using a 142 mega-pixel camera (Gunn et al. 1998), which gathers data in five passbands, u, g, r, i, z , spanning wavelengths $3000 \lesssim \lambda \lesssim 10,000 \text{ \AA}$. The photometric system and calibration are described in Fukugita et al. (1996); Hogg et al. (2001); Smith et al. (2002); Ivezić et al. (2004); Tucker et al. (2006). The astrometric calibration is described by Pier et al. (2003) and the data pipelines in Lupton et al. (2001). The Fourth Data Release (DR4) includes five-band photometric data for 180 million objects selected over 6670 square degrees, and 673,280 spectra of galaxies, quasars, and stars selected from 4738 square degrees of that imaging data using the standard SDSS target selection algorithms. Objects are selected from the imaging data for spectroscopy using a variety of algorithms. These include a complete sample of galaxies with reddening-corrected (Schlegel et al. 1998) Petrosian (1976) magnitudes brighter than $r = 17.7$ (Strauss et al. 2002).

2.2. Sample Selection

We use galaxies from the Main Galaxy Sample and have a redshift confidence of at least 0.7. We ignore objects with saturated pixels. We then exclude galaxies whose spectra has the Z_WARNING_NO_BLUE (no blue side of the spectrum) and Z_WARNING_NO_RED (no red side of the spectrum) flags (Stoughton et al. 2002). We then define a volume-limited sample through the further restrictions $0.019 < z < 0.125$ and $-23.5 < M_r < -20.5$. This gives a sample of 44,964 objects. For each object we obtain the atlas image (from the SDSS Data Archive Server), which comprises the pixels detected as part of each object in all filters. We use these images in the pixel-z analysis of the final volume-limited sample.

2.3. Galaxy Environment

We characterize the local density around each galaxy using a $5 \text{ Mpc } h^{-1}$ sphere centered on the galaxy in question. Each galaxy within that sphere is weighted according to the local completeness as calculated by Blanton et al. (2005) to account for spectroscopic fiber

collisions. Likewise, we scale the volume of the sphere according to the fraction of the projected sphere contained within the survey area. Since we are using a volume limited sample, we do not need to correct for redshift distribution variations.

There are a few possible caveats associated with this method. Naturally, working in redshift space versus real space opens us up to the possibility of galaxies scattering out of our volume in high density regions where the peculiar velocities would be high and vice-versa in lower density regions. In addition, our calculation of the sphere volume is compromised somewhat by treating masked regions near the center of the projected sphere identically to those on the edges, despite the fact that the former would remove a larger volume from the sphere than the latter. Of these, the redshift distortions are more problematic; our sky coverage is sufficiently uniform that tests using an exact spherical volume were not significantly different from those using our method. However, given that redshift distortions are at least equally problematic for any density estimates working in redshift space (Dressler 1980; Gómez et al. 2003), we feel that the more physically-based aspect of our method makes it the preferred approach. Figure 1 shows the distribution of local galaxy densities in our sample.

3. The method

3.1. pixel-z

By making use of strong spectral features such as the 4000 Å break, the Balmer break and the Lyman decrement, the standard photometric redshift techniques can be used to quickly provide an estimate of a galaxy’s redshift. Each SED is systematically redshifted, convolved with the photometric filter response functions, and compared with the observed fluxes through each filter. In the pixel-z method, however, we assume a redshift and fit for the SED type. In fact, for the SDSS Main Galaxy Sample, all galaxies have measured spectroscopic redshifts, so z can therefore be fixed in the fitting function. The best-fitting template is then established for each pixel at that particular redshift. The fitting function has the form:

$$\chi^2(T) = \sum_{i=1}^{N_f} \frac{[F_{\text{obs},i} - b_j \times F_{i,j}(T)]^2}{\sigma_i^2} \quad (1)$$

$F_{\text{obs},i}$ is the flux through the i th filter, b_j is a scaling factor, $F_{i,j}$ is the flux through the i th filter of the j th spectral energy distribution template (calculated at redshift z) and σ_i is the uncertainty in the observed flux. The sum is carried out over all available filters N_f . The resulting χ^2 is minimized as a function of template T providing an estimate of its spectral

type (together with the variance on this measure). Minimizing χ^2 in equation 1 with respect to b_j gives

$$b_j(T) = \frac{\sum_{i=1}^{N_f} \frac{F_{\text{obs},i} F_{i,j}(T)}{\sigma_i^2}}{\sum_{i=1}^{N_f} \frac{F_{i,j}(T)^2}{\sigma_i^2}}, \quad (2)$$

which determines the normalization of the SFR obtained from the best fitting SED template.

Rather than applying this technique to the integrated fluxes of galaxies, we instead apply it to the fluxes of pixels within resolved galaxy images. The individual pixels typically have larger photometric uncertainties than integrated fluxes measured in apertures, and careful account needs to be made of the uncertainties and error-propagation. The optimum solution would be to keep the spatial information present in the resolved image together with the improved signal-to-noise ratio offered by combining pixels. A step in this direction is indicated by Conti et al. (2003) (T. Budavári, 2003, private communication), where spatially connected pixels of similar colors are joined into *superpixels* in order to improve on the statistical errors without mixing the different galaxy components, such as a red bulge or bluer SF regions in spiral arms. Incorporating this technique into the current pixel-z implementation is beyond the scope of this investigation, but holds promise for future work.

By careful choice of the SED template library, the pixel-z technique enables a decomposition of the internal photometric structure of galaxies into basic constituents such as the age of the stellar population, their metallicities and their dust content. It enables, under simplifying assumptions, the determination of the SFR for individual pixels inside a galaxy, and the contribution of each pixel to the SFR of either the whole galaxy or a projected radial shell of that galaxy.

We have thus shifted the attention of the technique from the photometric redshift itself to the SED templates themselves. In fact, the SED of a galaxy should reflect the distribution of stellar masses, ages and metallicities and hence provide clues to the past history of star formation. By fitting SEDs to individual pixels in a galaxy, we can recover the morphological characteristics of the galaxy and separate the individual contributions of age, metallicity, dust and star formation history.

To verify our implementation of pixel-z and for comparison with the initial application to the HDFN by Conti et al. (2003), we test our method first on HDFN galaxies before moving to our SDSS sample. As in the analysis of Conti et al. (2003), we are able to connect features in the parameter maps (of age, SFR, obscuration, metallicity) of galaxies to individual morphological features such as knots of star formation that appear in the original images. The HDFN images have accompanying rms maps that quantify the uncertainty due to noise in the background. These maps were used to determine the detection significance of an object

or a pixel. No such maps are available for the SDSS galaxies. The photometric calibration of the SDSS imaging data (Atlas images) is done using the *asinh* magnitude system according to Lupton et al. (1999). The photometry is also corrected for foreground Galactic extinction using the extinction values obtained from the dust maps of Schlegel et al. (1998).

3.2. SED Templates

We use a large number of SEDs generated by the Bruzual & Charlot (2003) stellar population synthesis models. The main input parameters are the form of the SFR, the stellar initial mass function (we assume a Salpeter function with $M_l = 0.1 M_\odot$ and $M_u = 100 M_\odot$), and the rate of metal enrichment. The SEDs are normalized to a total mass of $1 M_\odot$. The input parameters for our SED templates are chosen to maximize our ability to solve for the above quantities. The SEDs have the following properties:

1. We allow the underlying stellar population within each pixel to vary over a wide age range. The age in the synthesis model is defined as the time since the most recent burst of star formation. We sample extremely young (0.001, 0.01, 0.1, 0.5 Gyr), to middle age (1, 3, 5 Gyr), to old and very old (9, 12, 15 Gyr), for a total of ten ages.
2. We assume that the fluxes of individual pixels can be modeled using an exponentially declining SFR with an e -folding timescale τ , i.e. $\Psi(t) = \Psi_0 e^{(-t/\tau)}$. This parameterization is convenient for its simplicity in describing the SFR of an instantaneous burst when $\tau \rightarrow 0$ and a constant SFR when $\tau \rightarrow \infty$. The e -folding times we use for τ range from 0.1 Gyr for a short burst, to 1, 3, 5, 9 and 12 Gyr for subsequently longer bursts. It is worth noting at this point that an exponential SFR for individual pixels does not inevitably lead to an exponentially decaying SFR for the galaxy as a whole, other than in the special case in which every pixel in the galaxy is coeval and all have the same SFR.
3. Since pixels with any SF history can be expanded in a series of instantaneous bursts, each having fixed metallicity, the spectral evolution of individual pixels (or whole galaxies) can be investigated without prior knowledge of chemical evolution. We assume the SEDs to be characterized by six possible metallicities spanning $\frac{1}{50}$ to 2.5 solar.
4. The general spectral characteristics of the SEDs of galaxies will be modified by the presence of dust. We parameterize dust obscuration in terms of the relative optical extinction in the rest frame $E(B-V)$ using the reddening curve $k(\lambda) = A(\lambda)/E(B-V)$, for star-forming systems formulated by Calzetti et al. (2000). For each of the SEDs we

allow for six independent values of extinction ranging from no extinction to $E(B-V) = 0.9$ magnitudes of extinction.

4. Pixel-z Implementation

We fit 2160 SED templates to all pixels in each of the SDSS galaxies in our sample, keeping the redshift of all pixels fixed to the spectroscopic redshift of their host galaxy. As discussed earlier, this effectively removes one degree of freedom in the fit and returns the properties of each of the pixels in terms of their best-fitting template, i.e. the age, SFR e -folding time, dust obscuration and metallicity. The normalization of the SFR in each pixel is based on the scale factor b_j which gives the SFR in units of $M_{\odot} yr^{-1}$. The total SFR for each galaxy is calculated from the sum of all pixels in the galaxy. We construct both unweighted and weighted sums to give a total star formation rate for the galaxy, where the weights correspond to the reciprocal of the square of the fractional error on the SFR in each pixel. The weighting is done to avoid giving undue significance to poorly constrained pixels, such as pixels dominated by the sky background, so that these pixels do not bias our measurements. The unweighted results turn out to be qualitatively the same as the weighted ones, but with some quantitative differences.

In calculating the total SFR we remove the simplifying assumption used by Conti et al. (2003) that all the pixels are coeval, i.e that they share a common age over the whole galaxy. The assumption of common age simplifies the interpretation by removing a degree of freedom, and enabling a clearer vision of the interplay between the remaining fitted parameters. That approach was useful in the analysis of Conti et al. (2003) in comparing maps of SFR, dust obscuration and metallicity for each galaxy with the underlying morphology. This assumption, however, is not consistent with the galaxy formation scenarios we are testing, nor is it required for our current analysis, and so we dispense with it.

4.1. Galaxy Maps

The technique allows us to probe not only the underlying morphological details of the galaxy, but also the relation between a galaxy’s morphology and its physical constituents.

The first two panels of Figure 2 show the results of the decomposition for two galaxies. The image on the left of the top panel shows a SDSS spiral galaxy, NGC 450 (SDSS J011530.44-005139.5) and the middle image shows the distribution of best fitting stellar population ages in Gyr throughout this galaxy. We see an older population in the nucleus of the

galaxy (ranging from 5-12 Gyr). In the outskirts there is a younger population, whose ages range from 0.001 to 0.2 Gyr. The distribution of this parameter also traces out some of the spiral arm structure. Around the inner spiral arms, some of the “knots” of star formation seen in the original r' band image can be detected in the age image too as yellowish-green regions (with ages between 0.1 and 2 Gyr). The bottom panel shows the results for an edge-on disk galaxy. We detect an older population in the nuclear region (around 12 Gyr) and a mix of intermediate (2-5 Gyr) and old populations (5-12 Gyr) elsewhere in the disk. The stellar populations in the outskirts have a comparatively younger age.

Figure 3 is a result of the template decomposition for another SDSS galaxy (SDSS J075642.69+364430.0). There is evidence for a bulge in this disk galaxy - the stellar populations are older - as much as 10 to 15 Gyr, whereas those in the disk are much younger, typically less than 1 Gyr. The population in the core also has lower e -folding time ($4 < \tau < 5$ Gyr) than in the outer disk. Together these results point to a lower current SFR in the central (bulge) population, compared to the disk population. The nucleus itself has a relatively low obscuration with $E(B - V) \approx 0.0$, while the stellar populations in the outer parts of the disk typically show a higher obscuration ($E(B - V) \approx 0.9$). The central part of the galaxy therefore shows an older population of stars, a faster timescale for SFR decline and a lower level of obscuration than the stellar populations in the outskirts of the disk. As we go further out we expect to be dominated by the sky pixels, which are artificially best fit by our SED templates corresponding to a younger stellar population, a longer timescale for SFR decline and a higher obscuration. Again, this artifact is identified through the large errors in the fitting, an important aspect of the pixel-z analysis, discussed in detail next.

4.2. Error Maps

The pixel-z method includes calculation of the intrinsic error arising from the SED fitting for each property characterizing the best fitting SED, as detailed by Conti et al. (2003). We provide a brief summary of the process here. Each pixel has a 4-dimensional likelihood function that results from fitting each of the 2160 templates to the five band fluxes in that pixel. In order to calculate the uncertainty associated with each of the four axes of variability (age, SFR e -folding time, obscuration and metallicity), we marginalize the likelihood over the three remaining parameters, essentially collapsing the four dimensional function along each of its axes. These likelihoods are sampled at the allowed values of each parameter. For example, the age likelihood is sampled at 10 different points corresponding to the 10 different ages.

The errors are then the 1σ uncertainties (corresponding to $\Delta\chi^2 = 1$) found by measuring

the width of the 1σ line that intersects the curve. Each pixel thus has uncertainties associated with each of the four parameters. In the top rightmost panel of Figure 2, we display the relative error in the age of the stellar populations. The inner arms of the spiral galaxy have a higher relative error in the age than does the central bulge region. In the second galaxy in the lower rightmost panel, the central bulge region has a lower relative error in the age than does the disk region.

In Figure 4 the bulge region, which shows an older stellar population has a lower relative error in the age ($\frac{\Delta t}{t} \approx 0.1$) than the disk region which shows younger stellar populations with much higher relative uncertainties. These higher uncertainties correspond to lower flux pixels. The high values of these relative errors can be reduced somewhat by finer sampling of the age parameter near the low best-fitting age value. Now beyond the disk, the pixel-z technique artificially fits to the sky background, so that the seemingly lower values of the relative error on the age parameter in the outermost pixels are an artefact of the fitting and could also be a product of template degeneracy (discussed below). However, in either the disk or the sky, pixels with a relative error > 1 will have a negligible contribution to the calculated SFR compared to those with very low relative errors.

The bulge also shows a faster e -folding time for star formation, with a lower relative error ($0 < \frac{\Delta \tau}{\tau} < 0.4$) than in the disk ($\frac{\Delta \tau}{\tau} > 1.0$). The pixels in the outer regions within the galaxy generally show the highest relative errors associated with the age and e -folding time. This emphasises that calculation of total or local SFR has to be weighted by these fitting uncertainties. Similar trends are seen in other parameters though the bulge population in the obscuration map has a higher relative error in the obscured flux (with $10^{0.4(\Delta E(B-V) - E(B-V))} \approx 1.2$) than does the disk (≈ 0.5), although the relative error becomes large again in the furthest outskirts of the galaxy.

In calculating either the total SFR of the galaxy, or the mean SFR in radial shells, we weight the SFR in each pixel by its relative uncertainty as calculated from the error maps for the age and τ parameter. The weight of each pixel is proportional to the reciprocal of the fractional error squared in the calculated SFR of each pixel.

4.3. SED degeneracies

Another uncertainty in the method is introduced by the degeneracy between the different parameters. There is likely to be a correlation between the parameters that determine the best-fit SED. We can investigate these correlations by using the 2-dimensional marginalized likelihood function, i.e. collapsing the 4-dimensional function onto the two axes of interest.

Example results from this analysis are shown in Figure 5. The top panel shows the likelihood contours as a function of age and star formation rate e -folding time for a single central pixel in an SDSS galaxy. This is typical of the degeneracies seen in the fitting of most pixels. The near-elliptical contours indicate that these two quantities are not independent at least in the central region. The likelihood function is double-peaked, with the global maximum corresponding to a 3 Gyr old population and a 1 Gyr SFR e -folding time. As both these quantities are used in determining the star formation rate, we could expect a certain degeneracy in the calculated star formation rate. The bottom panel shows the degeneracy between age and metallicity in a central pixel of another galaxy, with the maximum corresponding to a 0.01 Gyr old populations and a $Fe/H \approx 0.01$. Although we have identified such degeneracies, we have not yet exhaustively analysed their impact through all pixels in all galaxies in the sample. The tests we have explored, though, suggest that their impact will be minimal averaged over large samples of varied galaxy types.

One of the effects of this can be seen directly in the images. Figure 6 shows the effect of constraining all the pixels to have a common age. The lower-right image corresponds to the case where no constraint was used and a fit in the full parameter space was done, but the right image shows the case where the common age assumption was used. The reduced number of degrees of freedom enables a more resolved distribution of central bulge and disk in this τ map. Some of these degeneracies represent real physical relationships between the parameters, such as the well know age-metallicity degeneracy, while others reflect the choice of templates. Our selected templates cover the majority of parameter space, and since the fitting is done simultaneously over all parameters, the existence of degeneracies between any two parameters is mitigated. A more detailed study of the effect of these degeneracies is underway and will be incorporated in future work.

5. SFR variation with local density

5.1. Total galaxy SFR as a Function of Local Galaxy Density for All Galaxies

We investigate how the distribution of galaxy SFRs changes as a function of the local (spherical) galaxy density. The total SFR in each galaxy is calculated as a weighted sum of the SFR over all the pixels in the galaxy, where the weights are inversely proportional to the square of the fractional uncertainties in the SFR of each pixel. The local environment is quantified by counting the number of galaxies in a $5 \text{ Mpc } h^{-1}$ radius sphere centered on each galaxy.

Figure 7 shows the variation of the SFR distribution with local density, the three lines

corresponding to the 25th, median and 75th percentiles of the SFR distribution. The fluctuations at low densities are characteristic of the size of the systematic uncertainties in these measurements. The SFR decreases with increasing density, with the greatest effect in the highest density environments, $> 0.05 \text{ (Mpc/h)}^{-3}$ (densities that correspond to the outskirts of rich clusters).

These results, consistent with the measurements of Lewis et al. (2002) and Gómez et al. (2003), suggest that the total SFR of galaxies in the SDSS is strongly correlated with local density. This is also in agreement with the predictions of various hierarchical galaxy formation models whereby SF in galaxies is suppressed as galaxies fall into more dense environments such as clusters. The range of local densities in our sample allows us track the total SFR in galaxies in a wide range of environments: from the cores of rich clusters and groups into the field. As detailed by Gómez et al. (2003), based on the SDSS Early Data Release and using $H\alpha$ EW as a measure of SFR, Figure 7 illustrates the effect of environment on SFR. The overall SFR distribution, essentially flat for low densities, shows a decrease or suppression in regions of higher density. The effect is most noticeable in the most strongly star-forming galaxies, i.e. those in the 75th percentile of the SFR distribution. This means that the skewness of the distributions decreases with increasing density. The “break” density, beyond which the SFR distribution falls rapidly to lower values, around $0.05 \text{ (Mpc/h)}^{-3}$, occurs well into the regime of rich clusters, the extreme tail of the galaxy density distribution. A comparison between the “break” density seen here using our density estimator and that measured by Gómez et al. (2003) will be explored in future work.

5.2. Effect of the Density-Morphology Relation: Total SFR-density Relation for Early and Late Type Galaxies

It is well established that in more dense environments the galaxy population becomes dominated by early-type galaxies. For example, Dressler (1980) through the study of 55 nearby galaxy clusters found that the fraction of elliptical galaxies increases and that of spiral galaxies decreases with increasing local galaxy density in all clusters. This indicates that the physical mechanisms that depend on the environment of each galaxy mainly affect the final configuration of stellar component. The density-morphology relation was also found in groups of galaxies. For example, Postman et al. (1984) using data from the CfA Redshift Survey, found that the density-morphology relation for groups is consistent with Dressler (1980). The relation was also observed in X-ray selected poor groups (Tran et al. 2001).

We seek to determine whether the SFR of galaxies of a given morphology are also affected by environment, i.e. whether the SFR-density relation holds regardless of morphology. We

thus split our sample into two broad morphological bins based on the (inverse) concentration index C i.e early-types with $C \leq 0.4$ and late-types with $C > 0.4$. Consequently, there are 27,993 early-type galaxies and 16,971 late-type galaxies. Figure 8 presents the distribution of SFR as a function of the local galaxy density for each of these morphological types. For early-types, the density-SFR relation is similar to the one observed for the full sample: the overall SFR distribution is relatively flat (compared to the size of systematic fluctuations) for low densities and then shifts to lower values beyond $0.05 (\text{Mpc/h})^{-3}$. Like the trend for the full sample, the decrease at higher densities is most noticeable in the most strongly star-forming galaxies in the 75th percentile of the SFR distribution, with a sharp decrease beyond $0.05 (\text{Mpc/h})^{-3}$. The scatter in the SFR distribution decreases with increasing galaxy density for early-types. For late-types, the overall SFR distribution is also relatively flat at low densities but then falls to lower values beyond $0.055 (\text{Mpc/h})^{-3}$. However, the 75th percentile of the SFR distribution for late-types does not decrease as sharply as for early-types at these higher densities i.e. the SFR of these high-SF late-type galaxies is higher than for the early-types in the same density regime. Finally, unlike the early-types though, the scatter in the relation is relatively unchanged for late-type galaxies across all densities.

The results are broadly consistent with the findings of Gómez et al. (2003) who also split their sample based on the parameter C . They found that early and late-type galaxies each obey a SFR-density relation, although it is a shallow one for early-types (which have low SFR) while for late-types (which dominate the galaxies in their sample with high SFR), the relation is similar to that for the full sample.

5.3. Radial variation of SFR as a function of Local Galaxy Density

Although we have established a correlation between the total galaxy SFR and galaxy density, we can now explore where within the galaxies this suppression is taking place. In particular, we are interested in finding out if the suppression is primarily in the outskirts of galaxies or if it is in their inner regions. The former would support the predictions of hierarchical (“infall and quench”) models of galaxy formation, as the SF in the outskirts of the galaxies would be expected to be first affected by encountering an increasingly dense environment, while the latter, as discussed in § 1.2, would favour an “environmentally governed evolution” scenario. By using pixel- z to study the spatial distribution of SF, we will be able to distinguish between these two models.

For each galaxy we calculate a weighted mean SFR Ψ_w within successive annuli:

$$\Psi_w = \frac{\sum_{i=1}^{N_a} w_i \times \Psi_i}{\sum_{i=1}^{N_a} w_i} \quad (3)$$

where w_i is the weight corresponding to Ψ_i , the SFR in pixel i , and N_a is the number of pixels within that annulus a . The weight w_i is inversely proportional to the square of the fractional error on the SFR for the pixel i . The SFR in each annulus is thus normalized by the number of pixels, accounting for the larger total SF at larger radii due to a greater number of pixels. Scaling the radius of each annulus by the Petrosian radius (R_p) of the galaxy allows us to stack annuli for different galaxies (which have different Petrosian radii) together. The center of the galaxy is chosen as the brightest pixel in the galaxy.

We examine the annular distribution of Ψ_w for the stacked galaxies, spanning a range of local densities: $0.0 < \rho \leq 0.01 \text{ (Mpc/h)}^{-3}$, $0.01 < \rho \leq 0.04 \text{ (Mpc/h)}^{-3}$, $0.04 < \rho \leq 0.09 \text{ (Mpc/h)}^{-3}$. Figure 9 shows the median and 75th percentiles of this distribution. The inner annuli are more finely binned with $\Delta(r/R_p) = 0.125$ for $r/R_p \leq 0.25$, while $\Delta r/R_p = 0.25$ for $r/R_p > 0.25$. Errors are calculated for each annulus by propagating the errors in all the SFRs Ψ_i of the pixels within that annulus. The typical size of $0.125r/R_p$ is 2-3 pixels. There are 2785 galaxies where $0.125r/R_p$ is below the pixel resolution. Removing these galaxies neither significantly changes the radial profile of SF nor affect its dependence on local density.

Star formation in galaxies on average is higher in the the mid-annular region than in the core or outskirts. It is lower (averaged over all morphological types and inclinations) in the nucleus than in the circum-nuclear regions. We find that in dense environments this low SF in the nuclear regions appears lower still. The higher SF in the circum-nuclear region ($0.125 < r/R_p \leq 0.25$) is also lessened in more dense regions. It is this depression in the innermost annuli that accounts for the dependence of total galaxy SFR on density.

The effect can be seen most prominently in the 75th percentile of the distribution of Ψ_w . The density dependence in the 75th percentiles of Ψ_w is most evident in the first two innermost annuli up to $r/R_p = 0.25$, where there is a clear suppression of Ψ_w between the lowest and highest density intervals: by $8.2 \times 10^{-4} M_\odot \text{ yr}^{-1}$ (with 4σ significance) in the nuclear region and $2.6 \times 10^{-3} M_\odot \text{ yr}^{-1}$ (with 3.5σ significance) in the circum-nuclear region. Beyond $r/R_p = 0.25$ there appears to be no clear dependence of the mean SFR on the local density of galaxies. We see a similar, though less pronounced, trend in the median of the distribution of Ψ_w . Again, there is no statistically significant dependence of the mean SFR on local density in galaxy outskirts.

5.4. Radial variation of SFR with Environment for High and Low Star Forming Galaxies

The suppression of the total galaxy SFR with increasing local density is most noticeable in the 75th percentile curve of Figures 7. In other words, at progressively higher densities, the distribution of galaxy SFRs is truncated at lower SFR values, and it is the population of the most highly star forming galaxies that are being affected. Here we investigate whether the radial variation we observe in Figure 9 is seen only in these high SFR galaxies, or whether such a trend also exists in more quiescent galaxies. We examine the galaxy populations comprising the upper and lower quartile of the SFR distribution, and the results are shown in Figure 10 for the high SFR galaxies (with $\text{SFR} > 1.02 M_{\odot} \text{ yr}^{-1}$) and in Figure 11 for the low SFR galaxies ($\text{SFR} < 0.32 M_{\odot} \text{ yr}^{-1}$). For the high SFR population, up to a radius of $0.25 R_p$, the suppression of mean SFR with environment is clearly evident, and as with the total galaxy population, there is no dependence beyond this radius. Again, as before, the effect is most pronounced for the 75th percentile of the mean SFR (in the range $0 < r/R_p \leq 0.25$), where there is a 2σ difference between the highest and lowest density intervals in the range $0 < r/R_p \leq 0.125$ and a 3σ difference in the range $0.125 < r/R_p \leq 0.25$. But it can also be seen in the median of the distribution (in the range $0.125 < r/R_p \leq 0.25$), where the difference is 2.5σ . This is consistent with the dependence of the radial variation of the mean annular SF with environment for the total galaxy population in the sample (averaged over all star formation rates) in §5.3.

For the low star forming galaxies a small, although not statistically significant, dependence on environment is seen. It is thus the population of strongly star forming systems that account for the observed relation between the radial mean SFR and local density of galaxies shown in Figure 9. The suppression of SFR in the innermost annuli of the most strongly star-forming systems accounts for the observed SFR-density relation in the overall galaxy population.

5.5. Physical Interpretation

In §5.1 and §5.2, we find evidence for a suppression of total SFR as we go to higher density environments, and this relation seems to be preserved independent of morphology. So the total SFR-density relation is a result of SFR suppression at higher densities, not just a result of the morphology-density relation (at least not solely). The suppression is evident at the highest densities, beyond $0.05 (\text{Mpc}/h)^{-3}$, in the regime of clusters. In these high density environments, there are a number of physical mechanisms responsible for the suppression of total SFR. These include ram-pressure stripping, galaxy harassment, and tidal disruptions,

mechanisms that are known to be dominant in cluster cores.

However, in §5.3, we find that the suppression of mean radial SF takes place in the cores of galaxies (particularly in the nuclear and circum-nuclear region) while the outskirts are not affected by their changing environment. This implies that the environment itself is not impinging on galaxies to suppress the SFR, as the outer regions should otherwise be most affected according to “infall and quench” models. Any physical mechanism cannot therefore be solely responsible for this drop in the nuclear SF. By extension, they cannot therefore be governing the suppression in total SFR in galaxies in high density environments.

This seems to point to an evolutionary rather than an environmental origin for the SFR-density relation. If galaxies in more dense environments formed their stars earlier and faster than those in less dense environments, that would be consistent with either a uniformly depressed SFR as a function of galaxy radius, or a depressed nuclear SFR, given that higher gas densities in the nuclear regions are likely to drive star formation more rapidly (supported by the fact that star forming disk galaxies typically show bulges dominated by old, red stellar populations).

These results seem to be consistent with the idea of “downsizing” in galaxy formation (Cowie et al. 1996), whereby the more massive galaxies form at earlier epochs. Downsizing is characterised by a decline in the mass of the galaxies that dominate the star-formation rate density with decreasing redshift (“downsizing of star formation”). This is supported by recent measurements of star-formation histories in both local galaxies from the SDSS (Heavens et al. 2004) and distant galaxies from the Gemini Deep Deep survey (Juneau et al. 2005). This is distinct from the “downsizing with quenching” which follows a different timescale - spheroidal galaxies have been known to have a second star-formation timescale, namely that of “quenching”: it becomes easier to keep galaxies gas-free with time. In fact, recent studies of the galaxy luminosity function at $z \approx 1$ (Bell et al. 2004; Faber et al. 2005) conclude that massive red galaxies observed at $z \approx 0$ migrated to the bright end of the red sequence by a combination of two process: the quenching of star formation in blue galaxies and the merging of less-luminous, previously quenched red galaxies. Faber et al. (2005) conclude that the typical mass at which a blue, star-forming galaxy is quenched (and therefore enters the red sequence) decreases with time. Our radial result is evidence for the “downsizing of star formation” as opposed to this “downsizing with quenching”.

In §5.4, we have also found that whereas the quiescent galaxies (corresponding to the bottom quartile of the total SFR distribution) in the sample show no significant dependence of SFR on environment at any radius, the radial dependence of the mean annular SFR for the highest star-forming galaxies (top quartile of the total SFR distribution) mirrors the trend for the full sample. In addition, while the decrease of total SFR with density is dominated

by the high-SFR galaxies, the quiescent galaxies show hardly any dependence of their total SFR on environment. The radial result in § 5.4 confirms that the total SFR-density relation is largely due to the decline of nuclear SF in these high SF galaxies as we go to higher density environments. The overall radial result can therefore be explained if we consider a population of active, star-forming galaxies which formed at high redshift. The SF in this population of galaxies is dominated by the nuclear SF. Out of this population, the more massive systems which formed in more dense environments also formed their stars earlier and faster than those in less dense environments. By $z \approx 0$, this sub-population (which originated from more massive systems) has a lower nuclear SF than the sub-population which formed in less dense environments. This supports the idea that the “downsizing of star formation” in galaxies as described by Cowie et al. (1996) applies only to the actively star-forming galaxies in our sample.

It could also be possible that this SFR suppression in galaxy cores may be a consequence of feedback from an active galactic nucleus (AGN). In particular, if AGN feedback in more massive systems is more efficient than in lower mass systems, and since dense environments are known to host more massive galaxies on average (Dressler 1980; Postman et al. 1984) this could perhaps lead to preferential suppression of nuclear star formation in more dense environments. This mechanism could be explored further by looking into the mass dependence of the SFR suppression in galaxies, although this is beyond the scope of our current analysis. The radius out to which such a feedback mechanism could suppress SF also needs to be quantified. The complete explanation is expected to be a combination of this “downsizing” in SF together with more efficient AGN feedback in galaxies in more dense environments.

5.6. Future Work

Although the density-morphology relation is seen to be independent of the total SFR-density relation, the relationship between the density-morphology relation and the radial result has yet to be explored. We know that in addition to the nuclear SF declining in more dense environments, the location of the SF peak within galaxies is shifted to larger radii at higher densities. Is this telling us that the signal from early-type galaxies is just becoming stronger as we go to higher densities because there is a higher proportion of early types in those environments? At lower densities, the nuclear SF is higher, so could this be due to a predominance of late-types which are known to form in these low density environments? We know that by the “downsizing” argument, the more massive galaxies at high redshift form their stars early and rapidly. But these more massive systems tend also to be the elliptical galaxies, so to some degree, the radial trend (and its dependence on density) for

the full sample could still be, at least in part, a result of the density-morphology relation. To disentangle this, we wish to find out first what the radial SFR-density trends look like for each morphological type within our sample. Next, given these separate radial profiles, together with the fact that the proportion of early-type galaxies is expected to increase as we go to intervals of higher density, we wish to establish what the contribution of each type is to the radial SF-density trend for the full sample.

As discussed above in §5.4, we also know that it is indeed a sub-population of active, star-forming galaxies that is responsible for the trend of radial SF with environment. We wish to establish whether these systems are dominated by late-type galaxies or if they are a mixture of early and late-types. If this sub-population is indeed primarily late-type galaxies, then the radial SFR-density trend for late-type galaxies should mirror that of the high-SF population.

To further explore and support the “downsizing” idea, we also plan to extend this work to include an analysis on galaxies in a high redshift sample, from COSMOS (Koekemoer et al. 2007), GOODS (Giavalisco et al. 2004), or AEGIS (Davis et al. 2007). At high redshifts the high density environments are less evolved, and the relationship between SFR and density is likely to be quite different. Indeed, using GOODS data, Elbaz et al. (2007) has shown that the SFR-density relationship is inverted by $z \approx 1$, such that dense environments support enhanced, rather than suppressed, star formation. Using DEEP2 Galaxy Redshift Survey data, Cooper et al. (2006) also suggest that bright blue galaxies in overdense regions at high redshift have their star formation quenched and evolve into members of the red sequence by $z \approx 0$. These conclusions indicate that there exists a population of massive blue galaxies that has likely undergone quenching at $z \approx 1$, which has no high-mass counterpart today, and that there is a downsizing of the characteristic mass (or luminosity) at which the quenching of a galaxy’s star formation becomes efficient. They suggest that the quenching mechanism must operate efficiently in both cluster and group environments for consistency between their $z \approx 1$ and $z \approx 0$ results. Using pixel- z to explore the relationship between environment and the SFR distribution within galaxies at high redshift will aid in constraining the process by which such a mechanism might operate.

Lastly, we aim to explore the differences that may arise from using templates from a different stellar population synthesis model, in order to determine if the statistical results are in fact dependent on the model chosen and the different degeneracies that exist among the various parameters in that model. In future work, we aim to explore this issue using different models, such as PEGASE (Fioc & Rocca-Volmerange 2007).

6. Conclusions

Pixel-z is a useful technique for exploring spatially distributed galaxy properties, including the star formation rate. Although it has inherent limitations (detailed in this paper and by Conti et al. (2003)), it can provide insights to direct more detailed exploration, and when applied to large samples, many of those limitations can be overcome. We draw several conclusions about the environmental dependence of spatially resolved galaxy star formation:

1. By summing the SFRs in individual pixels, a total SFR-density relation is established. The SFR-density relation measured from emission lines (Gómez et al. (2003), Lewis et al. (2002)) is confirmed based on SFRs inferred from SED template-fitting to pixel fluxes across five bands.
2. The total SFR-density relation is found to be independent of morphological type of the galaxy. Therefore, the SFR-density relation of galaxies in the SDSS is not solely a result of having a larger fraction of early types as we go to higher densities (the morphology-density relation). So there is a SFR suppression in more dense environments.
3. Within galaxies, star formation, averaged over all morphological types and inclinations, is highest in a region spanning $0.125 \lesssim r/R_p \lesssim 0.5$, with the specific location of the peak depending on local density. It is lower in both the nucleus and the outskirts than in the circum-nuclear region. In denser environments, the low mean SFR in the nuclear regions appears lower still. The higher mean SFR in the circum-nuclear region is also lessened in more dense regions, with the peak SFR moving towards larger radii. The SFR beyond $r/R_p \approx 0.25$ and in the outskirts of galaxies is not affected by a changing environment. It is thus a depression of SF in the innermost annuli that accounts for the dependence of total galaxy SFR on density.
4. When the sample is split based on the total SFR of galaxies, it is the highly star-forming systems that are found to be responsible for the dependence of radial SFR on local density. The low star-forming galaxies show little dependence of radial SFR on environment.

7. Acknowledgements

NW would like to thank Tamás Budavári, Ravi K. Sheth, Ching-Wa Yip, Jeffrey Gardner, Simon Krughoff, Samuel Schmidt, Cameron McBride and Jeremy Brewer for useful discussions. AJC and NW acknowledge partial support from NSF grant ITR- 0312498 and

NASA AIRSP award NNG06GH97G. AMH acknowledges support provided by the Australian Research Council in the form of a QEII Fellowship (DP0557850). This material is based upon work supported by the National Science Foundation under the following NSF programs: Partnerships for Advanced Computational Infrastructure, Distributed Terascale Facility (DTF) and Terascale Extensions: Enhancements to the Extensible Terascale Facility.

Funding for the SDSS and SDSS-II has been provided by the Alfred P. Sloan Foundation, the Participating Institutions, the National Science Foundation, the U.S. Department of Energy, the National Aeronautics and Space Administration, the Japanese Monbukagakusho, the Max Planck Society, and the Higher Education Funding Council for England. The SDSS Web Site is <http://www.sdss.org/>. The SDSS is managed by the Astrophysical Research Consortium for the Participating Institutions. The Participating Institutions are the American Museum of Natural History, Astrophysical Institute Potsdam, University of Basel, Cambridge University, Case Western Reserve University, University of Chicago, Drexel University, Fermilab, the Institute for Advanced Study, the Japan Participation Group, Johns Hopkins University, the Joint Institute for Nuclear Astrophysics, the Kavli Institute for Particle Astrophysics and Cosmology, the Korean Scientist Group, the Chinese Academy of Sciences (LAMOST), Los Alamos National Laboratory, the Max-Planck-Institute for Astronomy (MPIA), the Max-Planck-Institute for Astrophysics (MPA), New Mexico State University, Ohio State University, University of Pittsburgh, University of Portsmouth, Princeton University, the United States Naval Observatory, and the University of Washington.

REFERENCES

- Abraham, R. G. 1998, in “The Ultraviolet Universe at Low and High Redshifts” (astro-ph/9802036)
- Balogh, M. L., Morris, S. L., Yee, H. K. C., Carlberg, R. G., & Ellingson, E. 1997, *ApJ*, 488, L75
- Balogh, M. L., Navarro, J. F., & Morris, S. L. 2000, *ApJ*, 540, 113
- Balogh, M. L. et al. 2004, *MNRAS*, 348, 1355
- Bell, E. F., McIntosh, D. H., Gyory, Z., Trujillo, I., Katz, N., Weinberg, M. D. 2004, *BAAS*, 204, 1403
- Blanton, M. R. et al. 2003, *ApJ*, 594, 186
- Blanton, M. R. et al. 2005, *AJ*, 129, 2562

- Boissier, S., et al. 2006, ApJS, (in press; astro-ph/0609071)
- Bruzual, G., Charlot, S. 2003, MNRAS, 344, 1000
- Byrd, G., Valtonen, M. 1990, ApJ, 350, 89
- Calzetti, D., Armus, L., Bohlin, R. C., Kinney, A. L., Koornneef, J., Storchi-Bergmann, T. 2000, ApJ, 533, 682
- Cole, S., Lacey, C. G., Baugh, C. M., Frenk, C.S. 2000, MNRAS, 319,168
- Conti, A., et al. 2003, AJ, 126, 2330
- Cowie, L. L., Songaila, A., Hu, E. M., Cohen, J. G. 1996, AJ, 112, 839
- Cooper, M.C., et al. 2006, MNRAS, 370, 198
- Couch, W. J., Balogh, M. L., Bower, R. G., Smail, I., Glazebrook, K., & Taylor, M. 2001, ApJ, 549, 820
- Davis, M., et al. 2007, ApJ, 660, L
- de Grijs, R., Lee J. T., Clemencia Mora Herrera M., Fritze-v. Alvensleben U., Anders P., 2003, NewA, 8, 155
- Dressler, A. 1980, ApJ, 236, 351
- Elbaz et al. 2007, A&A, 468, 33
- Faber, S. M., et al. 2005, (submitted to ApJ, astro-ph/0506044)
- Fioc, M., Rocca-Volmerange, B. 2007, A&A, 326, 950
- Fukugita, M., Ichikawa, T., Gunn, J. E., Doi, M., Shimasaku, K., Schneider, D. P. 1996, AJ, 111, 1748
- Giavalisco, M., et al. 2004, ApJ, 600, L93
- Gómez, P. L., et al. 2003, ApJ, 584, 210
- Gunn, J. E., & Gott, J. R. I. 1972, ApJ, 176, 1
- Gunn, J. E., et al. 1998, AJ, 116, 3040
- Gunn, J. E., et al. 2006, AJ, 131, 2332

- Hashimoto, Y., Oemler, A. J., Lin H., & Tucker, D.L. 1998, *ApJ*, 499, 589
- Heavens, A., Panter, B., Jimenez, R., & Dunlop, J. 2004, *Nature*, 428, 625
- Hogg, D. W., Finkbeiner, D. P., Schlegel, D. J., Gunn, J. E. 2001, *AJ*, 122, 2129
- Hogg, D. W., Blanton, M. R., Eisenstein, D. J., Gunn, J. E., Schlegel, D. J., Zehavi, I., Bahcall, N. A., Brinkmann, J., Csabai, I., Schneider, D. P., Weinberg, D. H., York, D. G. 2003 *ApJ*, 585, L5
- Hogg, D. W., Blanton, M. R., Brinchmann, J., Eisenstein, D. J., Schlegel, D. J., Gunn, J. E., McKay, T. A., Rix, H., Bahcall, N. A., Brinkmann, J., Meiksin, A. 2004, *ApJ*, 601, 29
- Ilbert, O., et al. 2006, *A&A*, 453, 809
- Ivezić, Ž., et al. 2004, *AN*, 325, 583
- Johnston, H. M., Hunstead, R. W., Cotter, G., Sadler, E. M. 2005, *MNRAS*, 365, 515
- Juneau, S., et al. 2005, *ApJ*, 619, L135
- Kauffmann, G., White, S.D.M., Guiderdoni, B. 1993, *MNRAS*, 264, 201
- Kassin, S. A., Frogel, J. A., Pogge, R. W., Tiede, G. P., Sellgren, K. 2003, *AJ*, 126, 1276
- Koekemoer, A. M. et al. 2007, *ApJS*, 172, 196
- Lanyon-Foster, M. M., Conselice, C. J., Merrifield, M. R. 2007, *MNRAS*, (in press; astro-ph/0706.2622v1)
- Lewis, I., et al. 2002, *MNRAS*, 334, 673
- Lupton, R., Gunn, J. E., Ivezić, Ž., Knapp, G. R., Kent, S. 2001, *ASPC*, 238, 269
- Lupton, R., Gunn, J. E., Szalay, A. 1999, *AJ*, 118, 1406
- Moore, B., Lake, G., Quinn, T., Stadel, J. 1999, *MNRAS*, 304, 465
- Panter, B., Jimenez, R., Heavens, A. F., Charlot, S. 2006, *MNRAS*, (submitted; astro-ph/0608531)
- Panter, B., Heavens, A. F., Jimenez, R. 2004, *MNRAS*, 355, 764
- Pérez-González, P. G., et al. 2006 *ApJ*, 648, 987

- Petrosian, V. 1976, ApJ, 210, L53
- Pier, J. R., Munn, J. A., Hindsley, R. B., Hennessy, G. S., Kent, S. M., Lupton, R. H., Ivezić, Ž. 2003, AJ, 125, 1559
- Poggianti, B. M., et al. 1999, ApJ, 518, 576
- Poggianti, B. M., et al. 2006, ApJ, 642, 188
- Postman, M., Geller, M. J., 1984, ApJ, 281,95
- Postman, M., Lubin, L. M., & Oke, J. B. 2001, AJ, 122, 1125
- Schlegel, D. J., Finkbeiner, D. P., Davis, M. 1998, ApJ, 500, 525
- Seymour, N., et al. 2007, (in preparation)
- Smith, J. A., et al. 2002, AJ, 123, 2121
- Somerville, R. S., & Primack, J. R. 1999, MNRAS, 310, 1087
- Stoughton, C., et al. 2002, AJ, 123, 485
- Strauss, M. A., et al. 2002, AJ, 124, 1810
- Tran K. H., Simard L., Zabludoff A. I., Mulchaey J. S., 2001, ApJ, 549, 172
- Tucker, D. L., et al. 2006, AN, 327, 821
- York, D. G., et al. 2000, AJ, 120, 1579

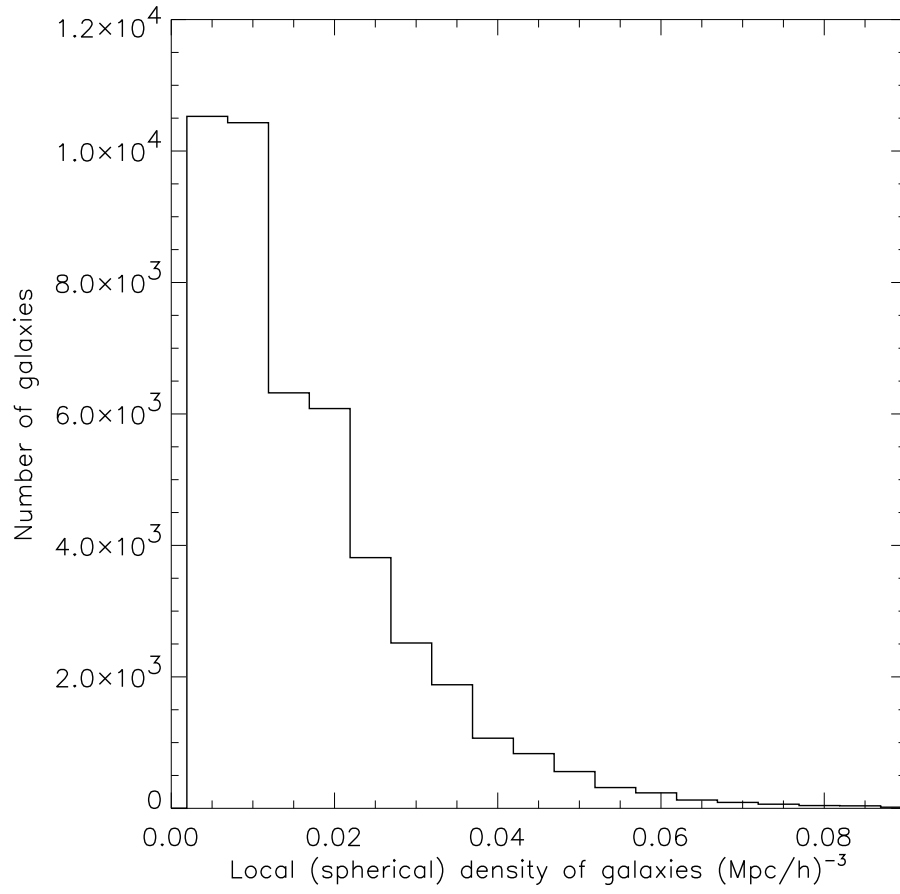


Fig. 1.— Density distribution of galaxies in the sample.

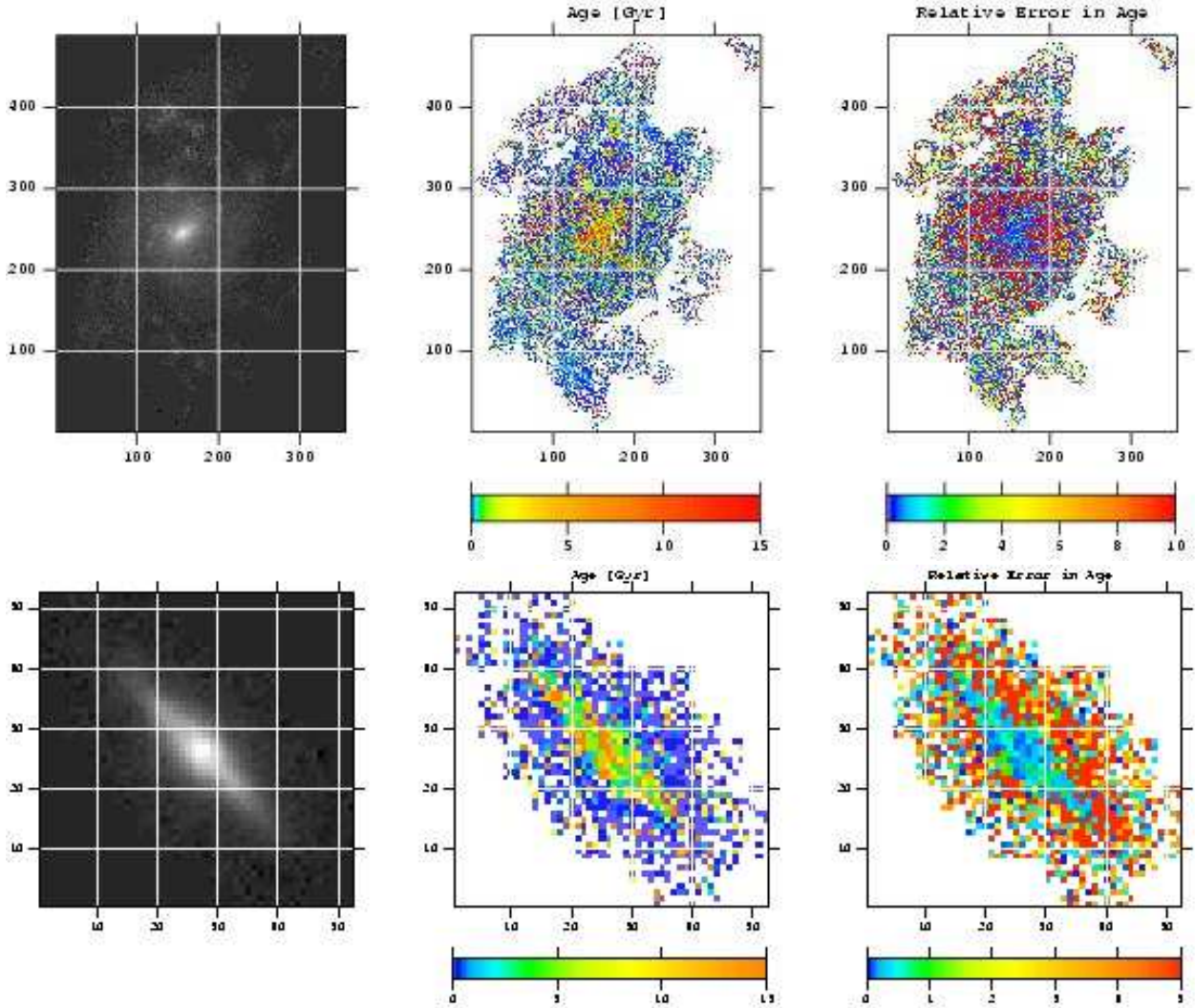


Fig. 2.— Top panel: Result of fitting 2160 SED templates to NGC 450 (SDSS J011530.44-005139.5) in the SDSS. The top left map shows the galaxy in the SDSS r' filter. The middle map displays the breakdown of the best-fitting template in each pixel according to the values of stellar population age in Gyr. Blue regions have the lowest age (0.001-0.1 Gyr), then green (0.1-0.6), then yellow (0.6-2 Gyr), then orange (2-7 Gyr), then red (7-15 Gyr). The third map shows the corresponding relative errors in the age for the pixels in this galaxy. As can be seen, the relative errors increase when going from the bulge region to the spiral arms. The map is obtained by computing the marginalized likelihood for each pixel in the galaxy as described in section 4. Bottom panel: Another galaxy (SDSS J155919.97+061729.8). The left image shows the image in the r' filter. The middle map is the age map and the right image is the corresponding relative error map on the age. The nuclear region, with high flux pixels, shows a lower relative error on the age but the disk has a higher relative error. A substantial number of sky pixels are captured on the outskirts of this galaxy. These have the highest relative errors.

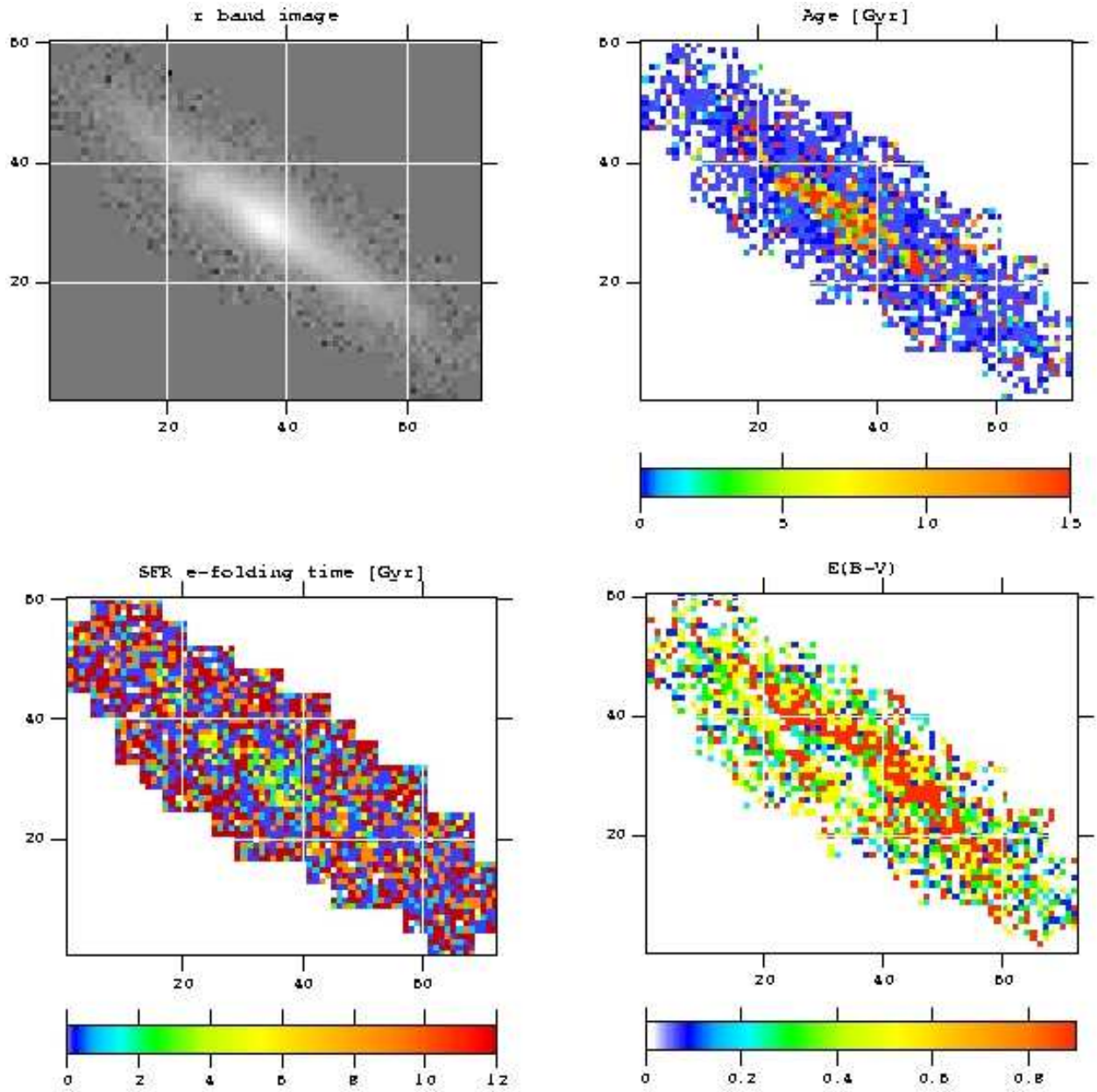


Fig. 3.— Result of fitting 2160 SED templates to each pixel in the SDSS galaxy SDSS J075642.69+364430.0. The top left map shows the galaxy in the SDSS r' filter. The other three maps display the breakdown of the best-fitting template in each pixel according to the values of the age of stellar population, star formation rate e-folding time in Gyr and color excess in magnitudes.

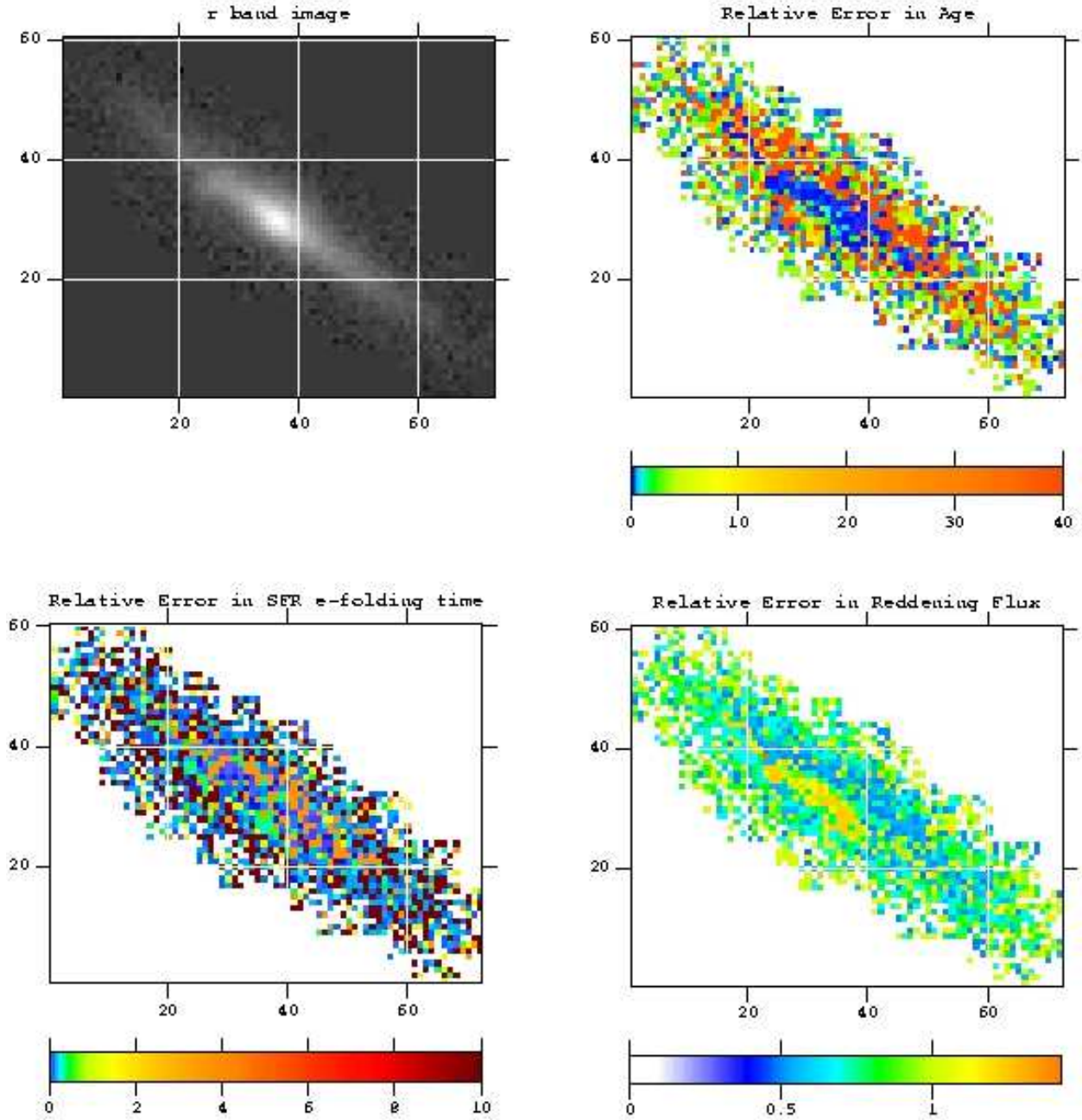


Fig. 4.— Relative error maps for the galaxy shown in Figure 3. Original image (top left), relative error in age (top right), relative error in SFR τ map (bottom left) and relative error in reddening flux $10^{0.4(\Delta E(B-V) - E(B-V))}$ (bottom right).

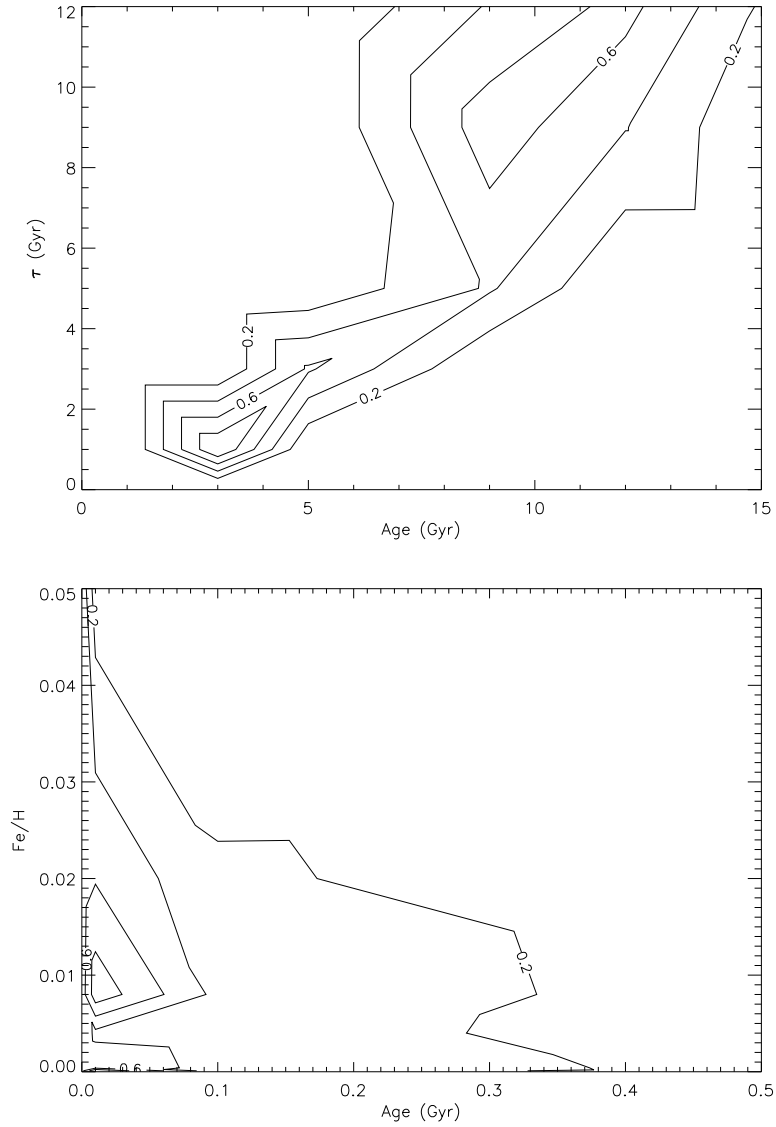


Fig. 5.— Top panel: Age- τ likelihood contours for a pixel in the nucleus of a galaxy. Bottom panel: Age-metallicity likelihood contours for a pixel in the nucleus of another galaxy. Contours are obtained from marginalizing the 4 dimensional likelihood function onto these two dimensions.

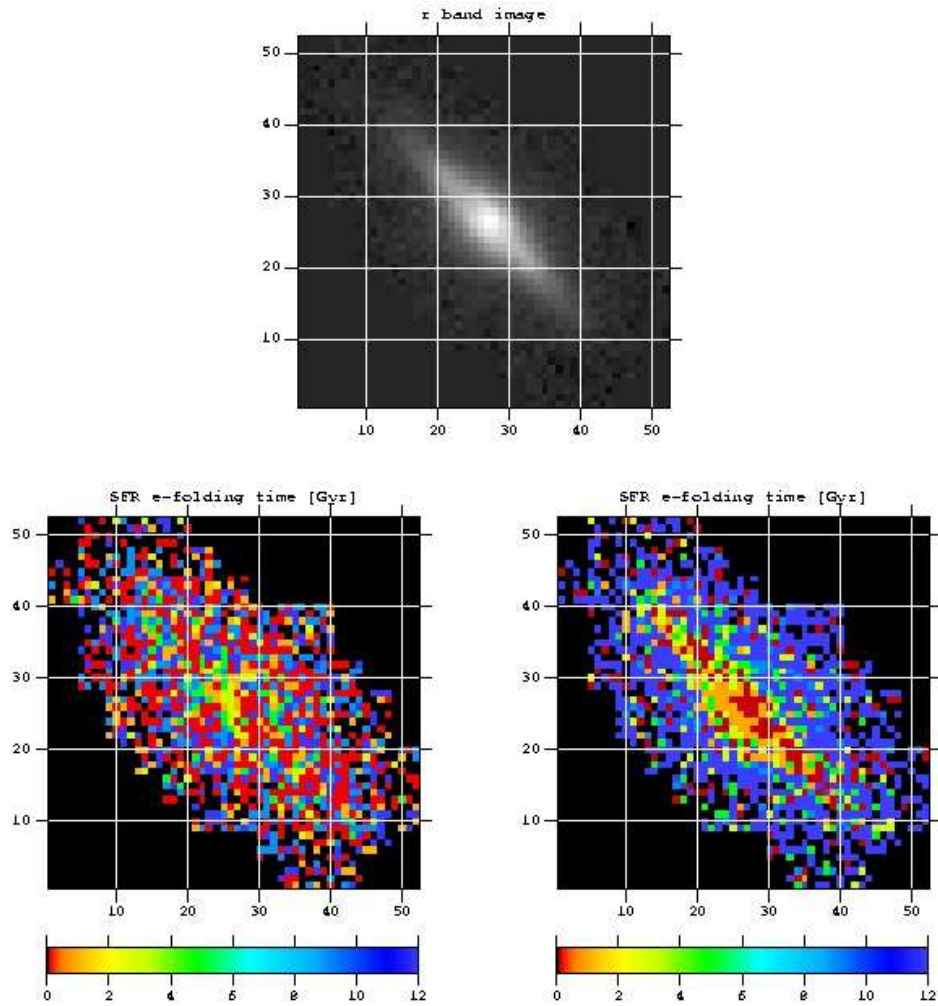


Fig. 6.— Effect of age- τ correlations. Top panel: Image of galaxy in the r' band. Lower-left panel: τ map. Lower-right panel: τ map where all the pixels are constrained to have a common age. The reduced number of degrees of freedom enables a more resolved distribution of central bulge and disk in this τ map.

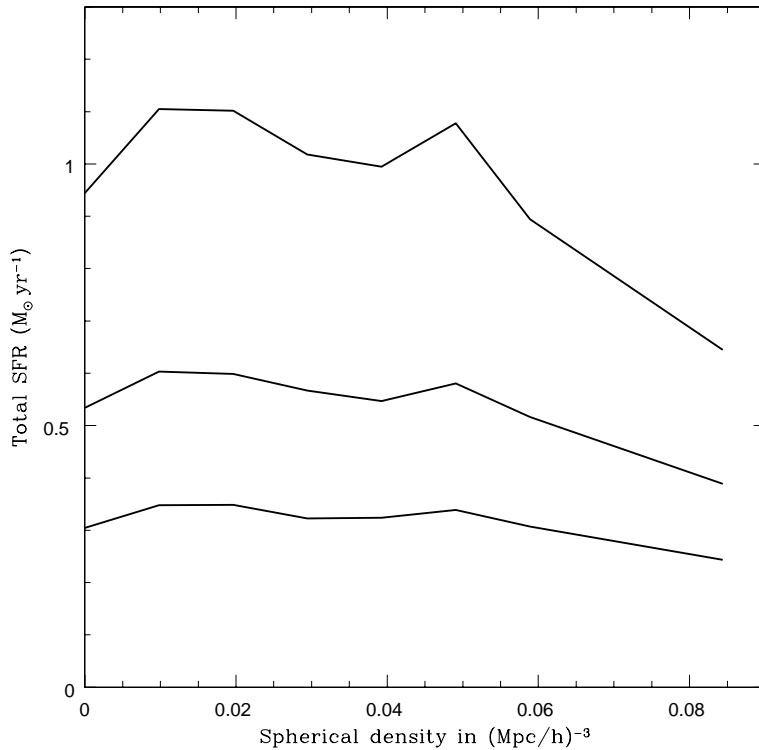


Fig. 7.— Galaxy SFR in $M_{\odot} \text{ yr}^{-1}$ as a function of density, where the SFR is calculated from a weighted sum over pixels in each galaxy. From top to bottom, the lines indicate the 75th, median and 25th percentiles of the SFR distribution respectively. The fluctuations at low densities correspond to the size of systematic uncertainties in the measurements. The overall SFR distribution which is essentially flat (given the size of these fluctuations) for low densities shifts to lower values at the higher densities. The decrease at higher densities is most noticeable in the most strongly star-forming galaxies, those in the 75th percentile. Finally, the range in the SFR distribution is largest at lower densities and decreases continuously with density.

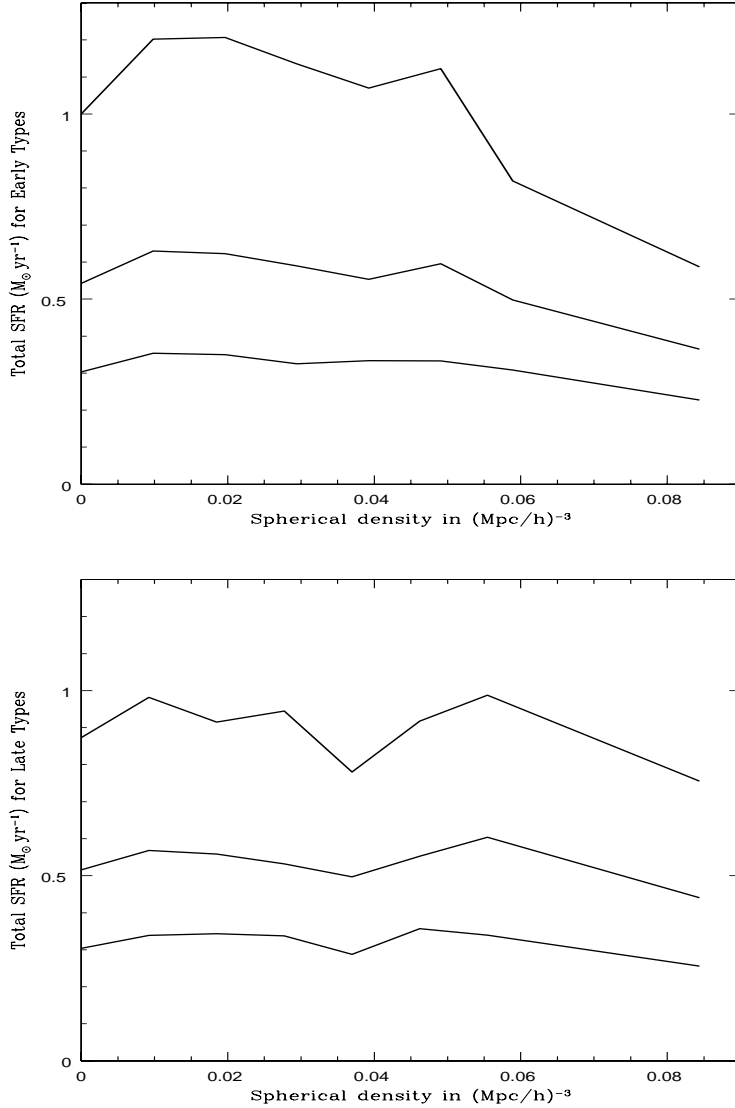


Fig. 8.— Top panel: SFR-density relation for early-type galaxies (with $C \leq 0.4$ as discussed in § 5.2). Bottom panel: SFR-density relation for late-types (with $C > 0.4$). In each panel, the total galaxy SFR is calculated from a weighted sum over pixels in each galaxy. From top to bottom, the lines indicate the 75th, median and 25th percentiles of the SFR distribution respectively. For early-types, the overall SFR distribution is relatively flat (compared to the size of systematic fluctuations) for low densities and then shifts to lower values beyond $0.05 \text{ (Mpc/h)}^{-3}$. The decrease at higher densities is most noticeable in the most strongly star-forming galaxies in the 75th percentile of the SFR distribution. For late-types, the overall SFR distribution is also relatively flat at low densities but then falls to lower values beyond $0.055 \text{ (Mpc/h)}^{-3}$. The range in the SFR distribution decreases with increasing galaxy density for early-types but is relatively unchanged for late-type galaxies.

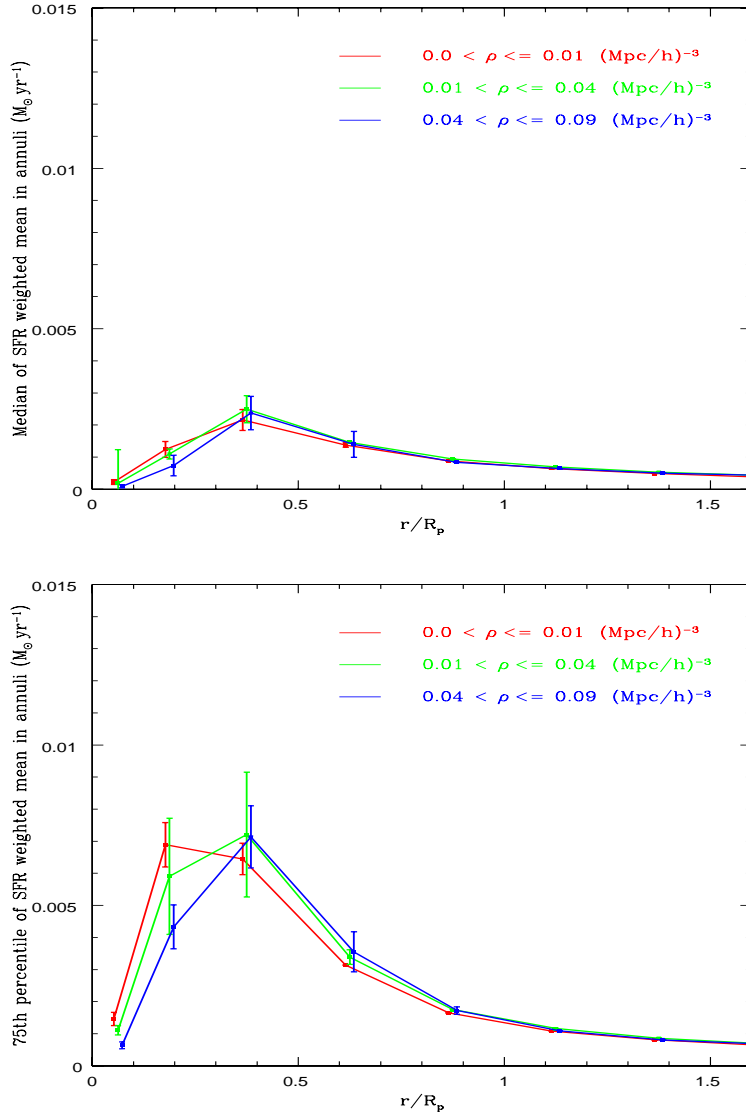


Fig. 9.— Top panel: Median of the weighted mean SFR Ψ_w ($M_\odot \text{ yr}^{-1}$) within successive radial annuli for 3 different intervals of galaxy density ρ : $0 - 0.01$ ($\text{Mpc}/\text{h})^{-3}$ (red), $0.01 - 0.04$ ($\text{Mpc}/\text{h})^{-3}$ (green), $0.04 - 0.09$ ($\text{Mpc}/\text{h})^{-3}$ (blue). Bottom panel: 75th percentile of Ψ_w ($M_\odot \text{ yr}^{-1}$). The mean SFR in each annulus for each galaxy is a weighted mean of the SFRs in all the pixels in the annulus. For galaxies in each local density interval, these radial annuli are then stacked. The percentiles are obtained from the distribution of the mean SFR in these stacked annuli. The inner annuli are more finely binned with $\Delta r/R_p = 0.125$, while $\Delta r/R_p = 0.25$ for $r/R_p > 0.25$. The density dependence in the 75th percentiles of Ψ_w is most evident in the first two innermost annuli up to $r/R_p = 0.25$, where there is a clear suppression of Ψ_w between the lowest and highest density intervals. The same is true to a lesser extent in the median. Beyond $r/R_p = 0.25$, no dependence on the local density of galaxies is detected.

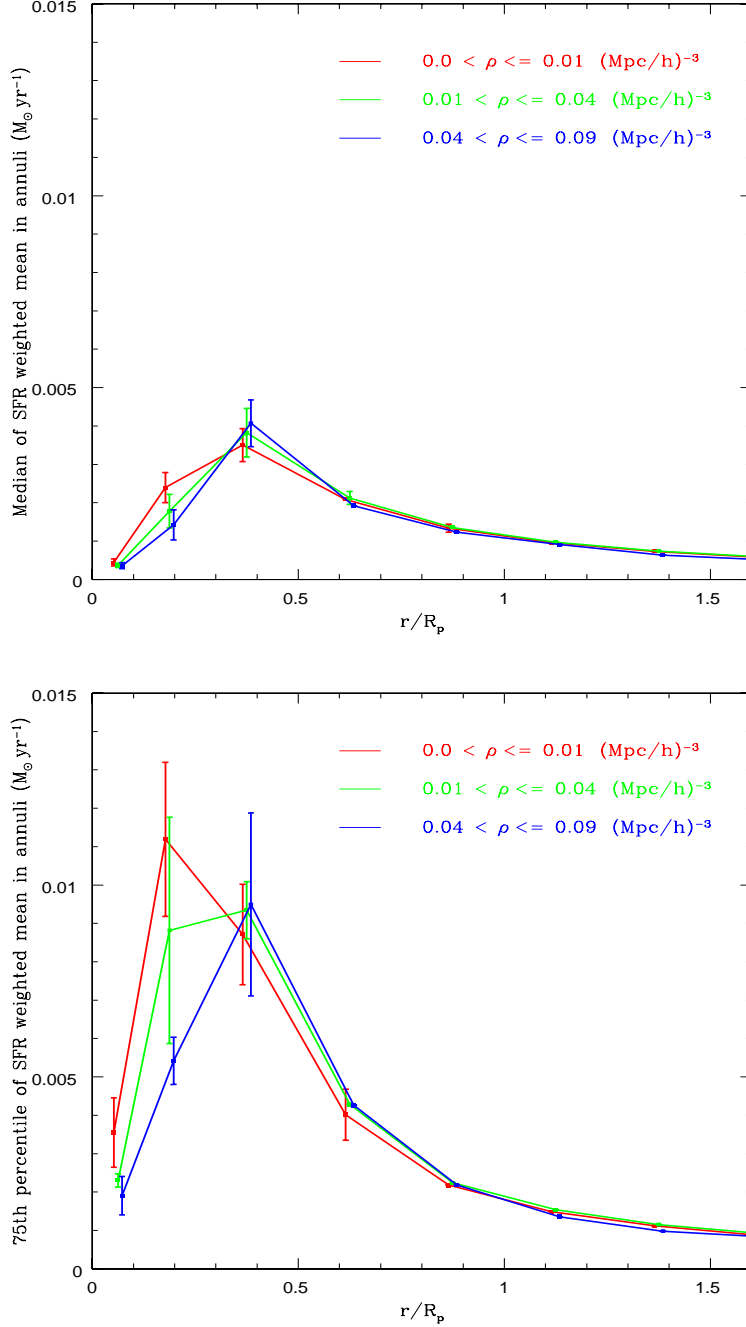


Fig. 10.— Top panel: Median of the distribution of weighted mean SFRs Ψ_w ($M_{\odot} \text{ yr}^{-1}$) within successive radial annuli as a function of the local galaxy density ρ for high star forming galaxies ($> 1.02 M_{\odot} \text{ yr}^{-1}$). There are 3 different intervals of ρ , as in Figure 9. Bottom panel: 75th percentile of Ψ_w ($M_{\odot} \text{ yr}^{-1}$).

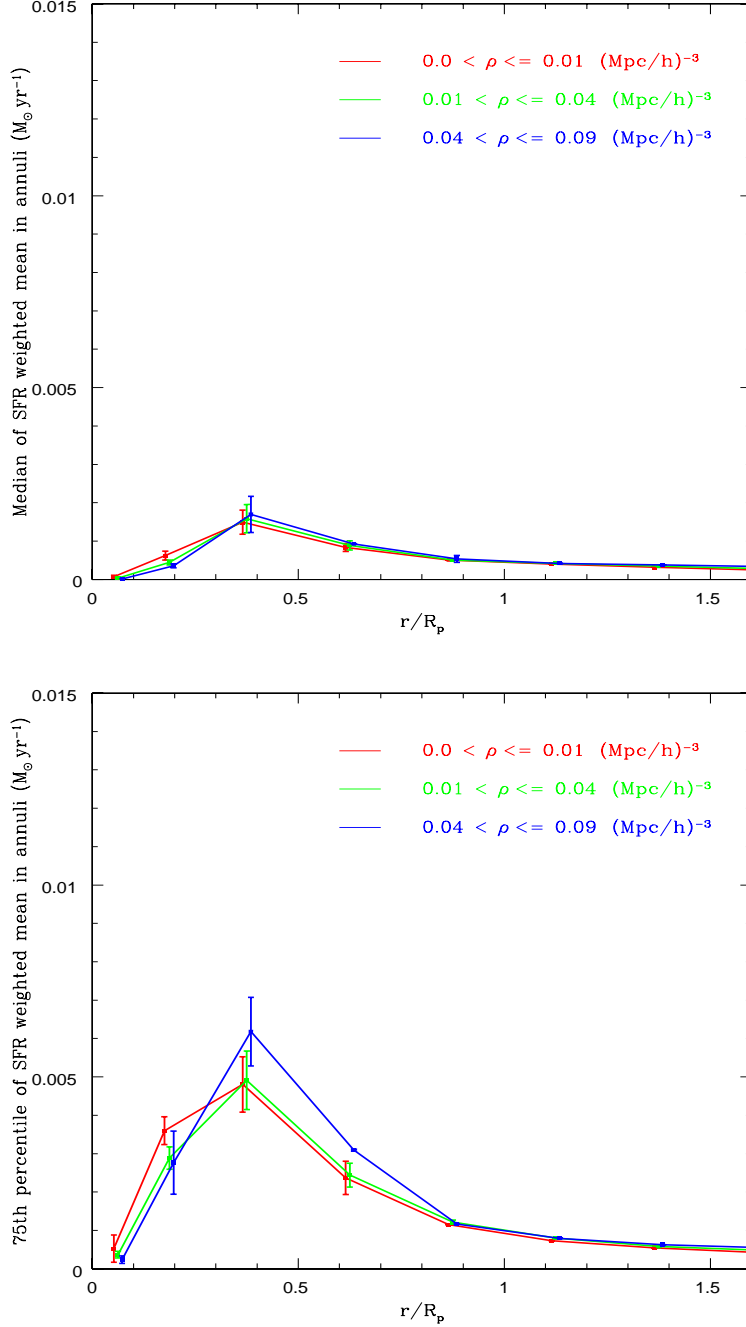


Fig. 11.— Top panel: Median of the distribution of weighted mean SFRs Ψ_w ($M_\odot \text{ yr}^{-1}$) within successive radial annuli as a function of the local galaxy density ρ for low star forming galaxies ($< 0.32 M_\odot \text{ yr}^{-1}$). There are 3 different intervals of ρ , as in Figure 9. Bottom panel: 75th percentile of Ψ_w ($M_\odot \text{ yr}^{-1}$).